Supplementary Figures

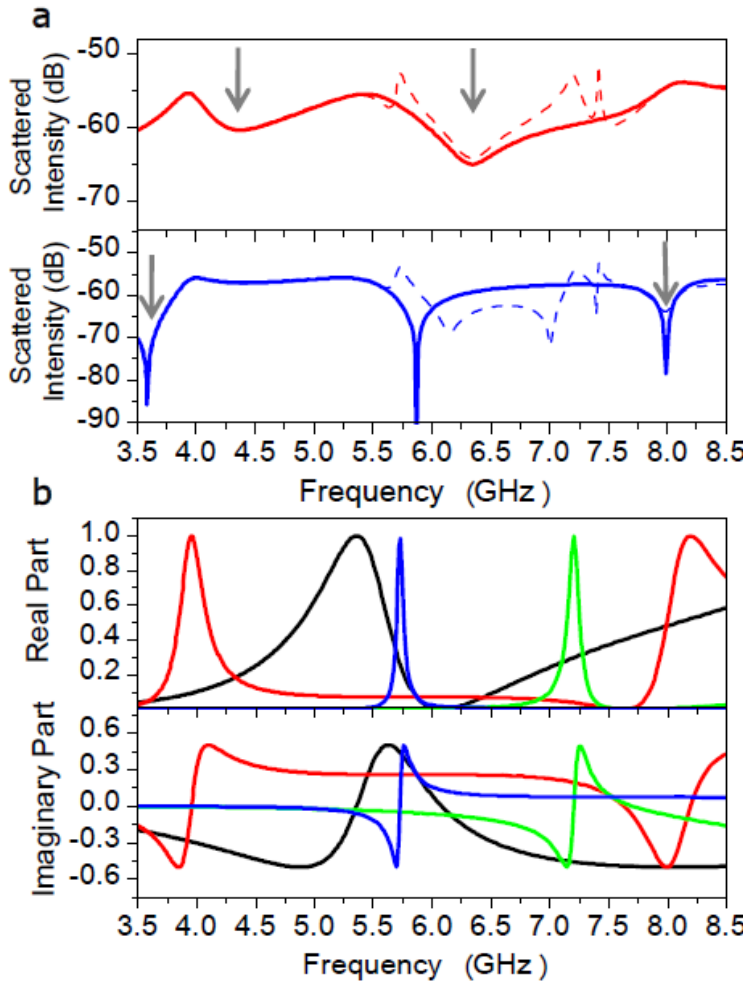

Supplementary Figure S1. Electromagnetic wave scattering in the forward and backward directions. a) *Simulated forward (upper part in red) and backward (lower part in blue) scattered intensities versus incident frequency (GHz), considering either a full Mie calculation (dashed line) or only the first two Mie terms (dipolar electric/magnetic) (continuous line) for a subwavelength dielectric particle (ε=16.5+0i, radius a=9mm). Kerker frequencies are marked with vertical arrows (i.e. coherent effects between the induced electric and magnetic dipole contributions at 4.3 GHz and 6.3 GHz in forward and 3.6 GHz and 8 GHz in backward). Two dips in the backscattered intensity also appear at 6.2 and 7 GHz whose main contribution is due to quadrupolar magnetic and electric Fano resonances from the interference of the Mie terms b_1-b_2 and a_1-a_2 respectively.* ***b)*** *Spectral evolution of both Real (top) and Imaginary (bottom) parts of the first four Mie coefficients corresponding to dipolar electric, a_1 (black), and magnetic, b_1 (red), and quadrupolar electric, a_2 (green), and magnetic, b_2 (blue), contributions. The behavior of the first four Mie coefficients, together with Eqs (10), helps to understand the interference effects shown in* ***(a)****.*

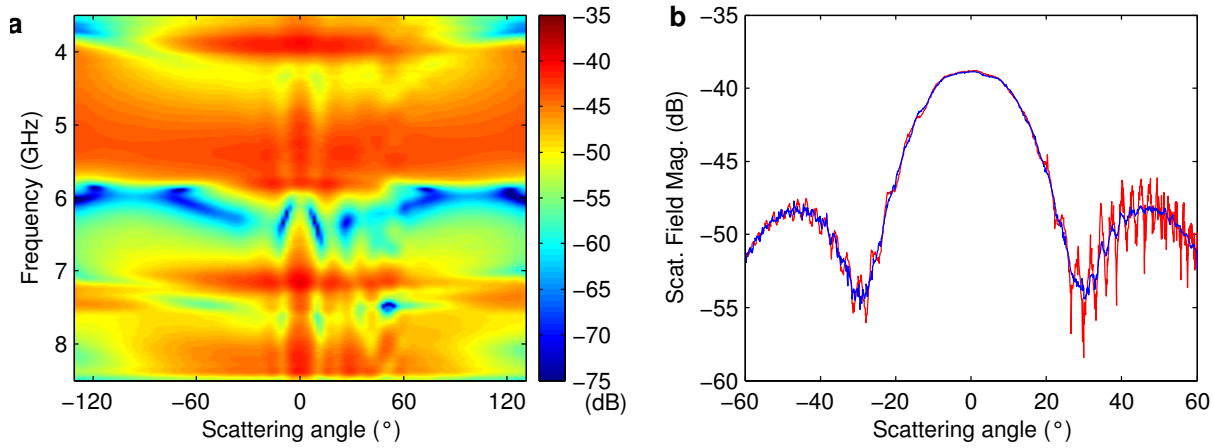

Supplementary Figure S2. Positioning errors. a) *Color map representation of the magnitude (dB) of the scattered field measured in the horizontal configuration as a function of receiver angle (°) and frequency (GHz),* ***b)*** *Magnitude of the scattered field of a 25 mm in radius PMMA sphere, measured clockwise (blue) and counterclockwise (red) at 10 GHz (λ=30mm).*

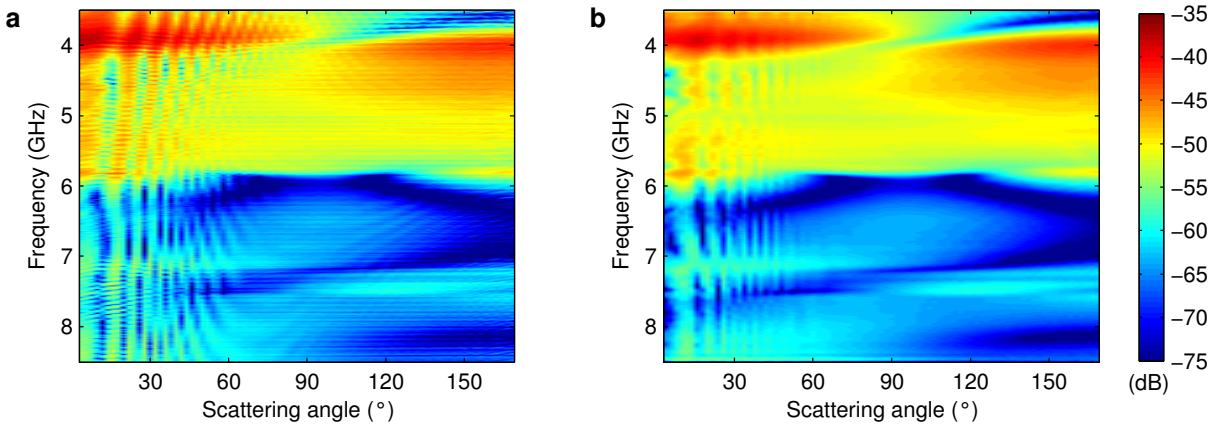

Supplementary Figure S3. Drift correction. a) *Color map representation of the magnitude (dB) of the raw measured scattered field before drift correction,* ***b)*** *after drift correction.*

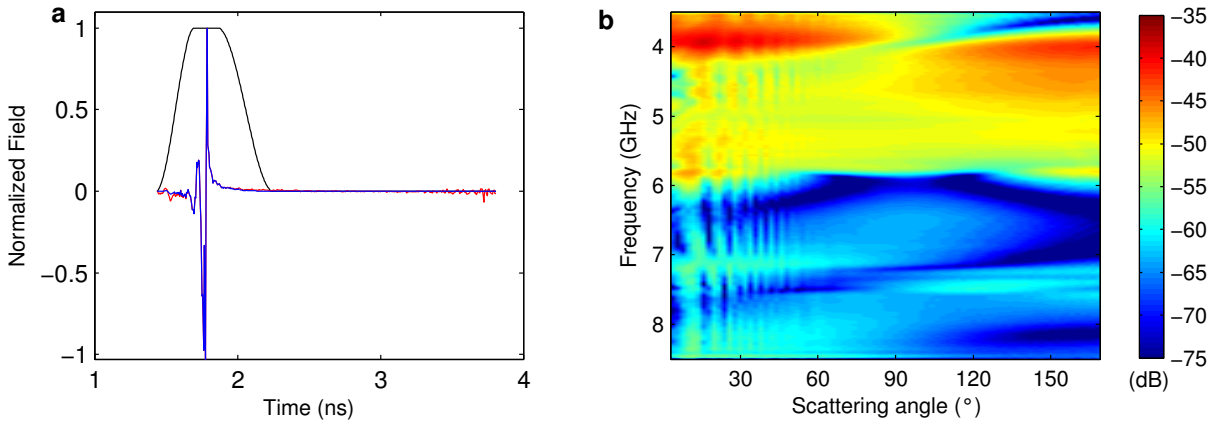

Supplementary Figure S4. Time gating. a) *Time gating applied to the scattered field (converted from the frequency domain to the time domain by Fourier transformation). Red line: real part of the scattered field for a given scattering angle (forward scattering in this case). Black line: shape of the used gate. Blue line: scattered field obtained after gating.* ***b)*** *Color map representation of the magnitude of the scattered field (dB) for every measured frequency and scattering angle (vertical configuration)*

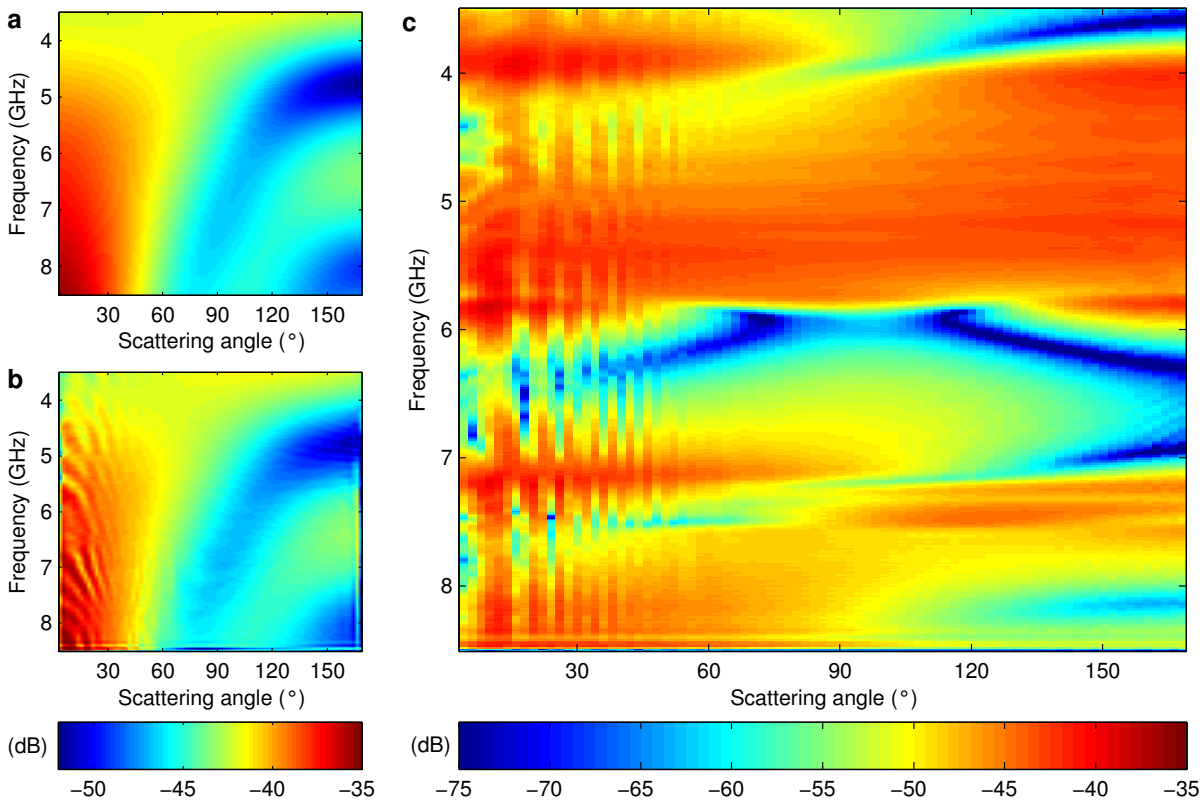

Supplementary Figure S5. Experimental calibration. a) *Color map representation of the magnitude (dB) of the Mie simulation of the field scattered by a 17.5 mm in radius metallic sphere,* ***b)*** *Measured scattered field for the same sphere,* ***c)*** *Calibrated scattered field.*

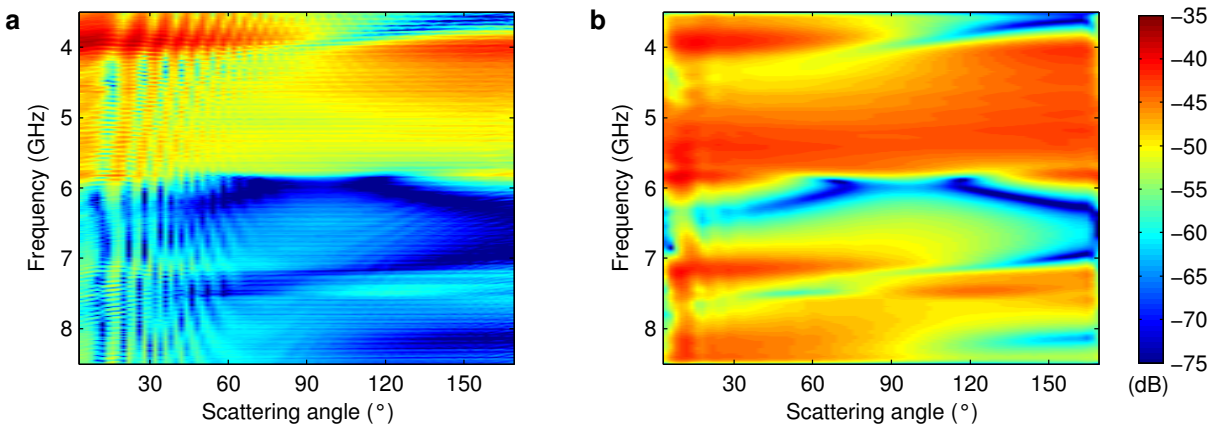

Supplementary Figure S6. Low pass filter. a) *Color map representation of the magnitude (dB) of the raw measured scattered field before any correction,* ***b)*** *after application of the full post-processing.*

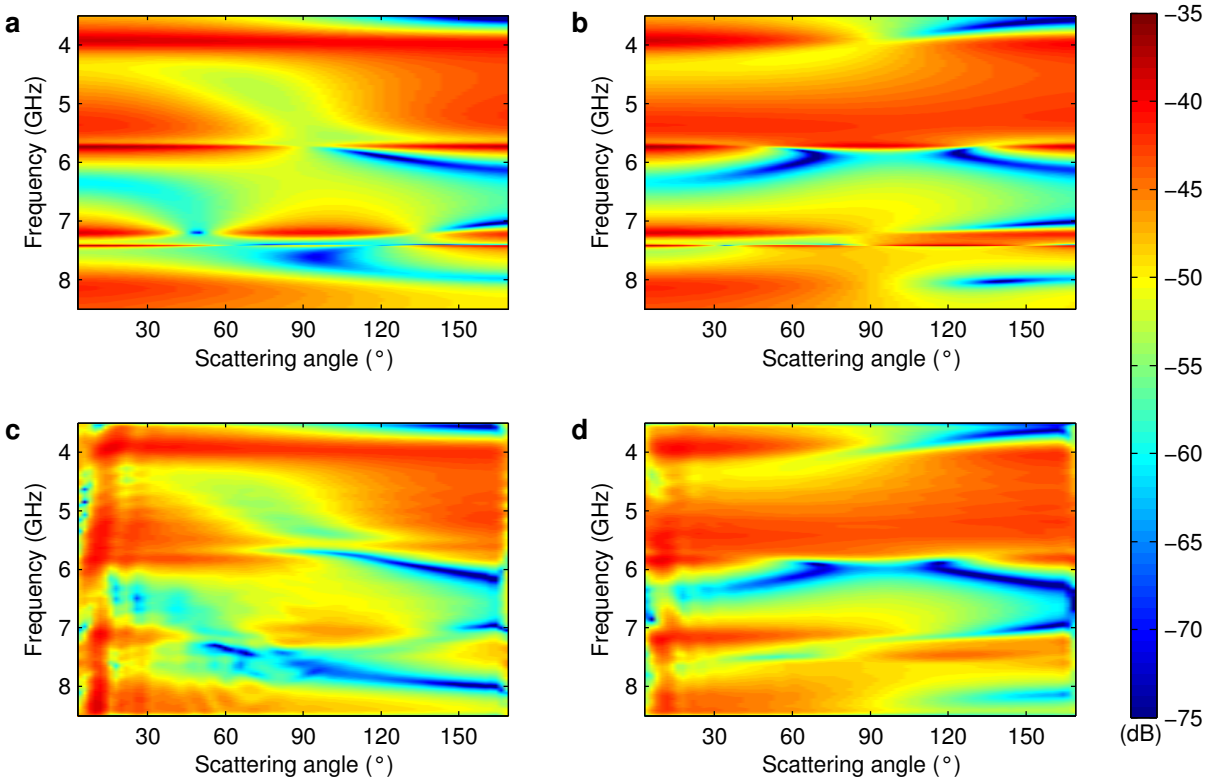

Supplementary Figure S7. Permittivity knowledge. a) *Color map representation of the magnitude (dB) of the Mie computed scattered field for P polarization,* ***b)*** *for S polarization,* ***c)*** *Color map representation of the measured and post-processed scattered field for P polarization,* ***d)*** *Color map representation of the measured and post-processed scattered field for S polarization.*

Supplementary Methods

Our experiments have been performed in an anechoic chamber at the Centre Commun de Ressources Microondes (Institute Fresnel, Marseille, France). This facility was successfully used for carrying out microwave analog to light scattering measurements on various kinds of complex particles [48-52]. The experimental set-up for measuring the electromagnetic properties (intensity/polarization) of the scattered wave by a single dielectric subwavelength sphere made of moderate high refractive index ($n = \sqrt{\varepsilon} \approx$3-4) is fully described in Fig. 1 of the main text. Due to the difficulty of those scattering measurements, in order to obtain reliable results, two types of post-processing of the data have been used, the first one compensates for the drift phenomenon, while the second one consists of a time gating filtering to remove as much as possible the stray signals [49]. The possible measurement error sources (positioning errors) and post-processing procedure are described in detail in this section.

***Positioning errors*.** In the horizontal configuration (HC), oscillations can be observed on the measured scattered fields (Supplementary Figure S2a) for the positive angles (especially between 30° and 50°). Those perturbations are due to repositioning inaccuracies of the receiving antenna. This is enlightened in Supplementary Figure S2b at the higher frequency of 10 GHz (λ=30mm) with a bigger sphere (25mm in radius) made of PMMA (ε = 2.6). Notice that, the scattered field cannot be measured directly but is obtained through the complex subtraction of the incident field (without any target) to the total field (in presence of the target). The incident and total fields having almost the same magnitude for some receiving positions, any difference in the absolute angular position of the receiver between those two measurements can lead to an important noise on the scattered field. This repositioning problem was in fact discovered when making the exact same measurements but moving the receiver once clockwise (as for the measured of the subwavelength sphere) and second counterclockwise (both done with a very small angular step, see Supplementary Figure S2b). The repositioning errors of the receiving antenna were estimated to be about one hundredth of a degree but this is enough to be visible on the scattered fields, especially with small targets for which the scattered field amplitudes are week (compared to the measured fields).

Post-processing procedure. Due to the very low levels of the scattered fields, a few post-processing techniques had to be applied to remove different kind of noises in the measurements. Unless specified otherwise, all the results presented in this paragraph are corresponding to the scattered field measured with a 9mm in radius sphere made of Eccostock HIK, K=16, [53] for the S polarization in the vertical measurement configuration.

Drift correction. The correction used to compensate for any drift phenomenon occurring between the measurement of the field with and without a target (total and incident fields) is based on the fact that the propagation of EM waves is a low pass filter [54]. The details are provided in [49]. Raw and drift corrected sample measurements are provided in Supplementary Figure S3.

Time gating. Despite the fact that all measurements were made in a continuous wave mode (CW), thanks to a Fourier transformation, it is still possible to remove stray signals using a time gating in the time domain. The procedure is very common, similar to those used in radar applications for example. Its only specificity comes from the fact that our targets are dielectrics analyzed in their resonance domain, thus it is rather difficult to find the optimal width of the gating function. Our choice was here to "wait" for the signal to reach 30dB under its peak value (see Supplementary Figure S4).

Calibration. To get quantitative results and furthermore to be able to compare the two polarization cases, we have to calibrate the measured values using reference data. To this aim, we make measurements on a well-known target, here a 17.5mm in radius metallic sphere, and compare them to Mie simulations (Supplementary Figures S5a and b). From this comparison we compute one single coefficient per frequency and apply it to every unknown target (see Supplementary Figure S5c for the 9mm in radius sphere made of Eccostock HIK and compare it with Supplementary Figure S4b [45]).

Low pass filter. Due to the fact that we a priori know the size of the target under test, the spectral bandwidth of its scattered far-field is theoretically limited (see [54] for example) to ka (k being the wave number and a the radius of the minimal sphere including the target). To be sure to keep all the available information, a $2ka$ filtering was used here. The result of the full post-processing of the raw data is given in Supplementary Figure S6.

Permittivity knowledge. The knowledge of the permittivity value of the target material is a key point when comparing measured scattered fields to simulated ones. In all the presented results the dispersion of the permittivity with respect to the frequency was assumed to be negligible (realistic in the 3.5 to 8.5 GHz frequency band (λ=35-86mm) with respect to our permittivity measurements), as the used material has a very small loss tangent angle (given to be 0.002 by Emerson & Cuming [53]) and since it was not possible to check it with confidence. As Emerson & Cuming [53] provides only a permittivity value at 10 GHz (λ=30mm), we estimated it for a slightly bigger sphere (radius: 12mm) made of the same material. This was done by comparing, for several frequencies, Mie simulations (without any losses) to experimental data. The permittivity was obtained from a minimization of the RMS difference between measured and computed fields. The resulting value is $\varepsilon = 16.5$ and was then used to compare measurements and simulations for the 9mm radius sphere case (Supplementary Figure S7) in the whole frequency range under consideration. Despite our limited experience with such high permittivity materials and such small targets, it can be seen that simulations and measurements compare quite well over the whole frequency range and for all the scattering angles.

Supplementary References

[50] Sabouroux P., Stout B., Geffrin J.-M., Eyraud C., Ayranci I., Vaillon R. & Selçuk N., Amplitude and phase of light scattered by micro-scale aggregates of dielectric spheres: comparison between theory and microwave analogy experiments, *J. Quant. Spectr. Rad. Trans.* **103**, 156-167 (2007).

[51] Merchiers O., Geffrin J.-M., Vaillon R., Sabouroux P. & Lacroix B., Microwave analog to light scattering measurements on a fully characterized complex aggregate, *Appl. Phys. Lett*. **94**, 181107 (2009).

[52] Merchiers O., Eyraud C., Geffrin J.-M., Vaillon R., Stout B., Sabouroux P. & Lacroix B., Microwave measurements of the full amplitude scattering matrix of a complex aggregate: a database for the assessment of light scattering codes, *Opt. Express* **18**, 2056–2075 (2010).

[53] http://www.eccosorb.com/

[54] Bucci O.M. & Isernia T., Electromagnetic inverse scattering: retrievable information and measurement strategies, *Radio Sci.* **32**, 2123-37 (1997)